J. Fluid Mech. (1997), *vol.* 338, *pp.* 59–87

Experiments on drag-reducing surfaces and their optimization with an adjustable geometry

By D. W. BECHERT[1], M. BRUSE[2], W. HAGE[2], J. G. T. VAN DER HOEVEN[3] AND G. HOPPE[4]

[1] DLR, Abteilung Turbulenzforschung, Müller-Breslau-Str. 8, 10623 Berlin, Germany

[2] Hermann-Föttinger-Institut, TU Berlin, Strasse des 17. Juni 135, 10623 Berlin, Germany

[3] Universitätsklinikum Rudolf Virchow, Klinikum Westend, Labor für Biofluidmechanik, Spandauer Damm 130, 14050 Berlin, Germany

[4] Deutsches Institut für Bautechnik, Kolonnenstr. 30, 10829 Berlin, Germany

(Received 10 January 1996 and in revised form 5 November 1996)

Previous research has established that surfaces with tiny ribs (riblets) aligned in the streamwise direction can reduce the turbulent wall-shear stress below that of a smooth surface. Typical skin-friction reductions have been found to be about 5%. The results of the present investigation, however, demonstrate a considerable improvement over this value. This improvement is achieved by a systematic experimental optimization which has been guided by theoretical concepts.

A key feature of our experiments is the utilization of an oil channel. Previous experiments in wind tunnels had to contend with very small riblet dimensions which typically had a lateral rib spacing of about 0.5 mm or less. By contrast, in our oil channel, the ribs can have a lateral spacing of between about 2 and 10 mm. This increased size of the surface structures enables test surfaces to be manufactured with conventional mechanical methods, and it also enables us to build test surfaces with adjustable geometry. In addition, the Berlin oil channel has a novel shear stress balance with an unprecedented accuracy of $\pm 0.3\%$. This latter feature is a prerequisite for a systematic experimental optimization.

In the present investigation, surfaces with longitudinal ribs and additional slits are studied. The experiments cover a fairly large range of parameters so that the drag reduction potential of a surface with ribs and/or slits is worked out conclusively. A large parameter range is made possible because of the adjustability of the surfaces as well as the automatic operation of the oil channel. In particular, the following tests were run:

(i) Shear stress measurements with conventional riblet configurations, i.e. with triangular and semi-circular grooves, have been carried out. These measurements were necessary in order to establish the connection between our oil channel data and previous data from wind tunnels. As was previously established, we found a drag reduction of about 5%.

(ii) An adjustable surface with longitudinal blade ribs and with slits was built and tested. Both groove depth and slit width could be varied separately and continuously during the experiment. It turned out, that slits in the surface did not contribute to the drag reduction. Nevertheless, these investigations show how perforated surfaces (e.g. for boundary-layer control) can be designed for minimal parasitic drag. On the other hand, with closed slits, an optimal groove depth for the rib surface could be determined, i.e. half of the lateral rib spacing. For this configuration, we found an 8.7% skin-friction reduction. By carefully eliminating deleterious effects (caused by

little gaps, etc.), the skin-friction reduction could be improved to a record value of 9.9%.

(iii) A quantitative comparison between theory and experiment was carried out. The theory is based on the assumption that riblets impede the fluctuating turbulent crossflow near the wall. In this way, momentum transfer and shear stress are reduced. The simplified theoretical model proposed by Luchini (1992) is supported by the present experiments.

(iv) For technological applications of riblets, e.g. on long-range commercial aircraft, the above thin-blade ribs are not practical. Therefore, we have devised a surface that combines a significantly improved performance (8.2%) with a geometry which exhibits better durability and enables previously developed manufacturing methods for plastic riblet film production to be used. Our riblet geometry exhibits trapezoidal grooves with wedge-like ribs. The flat floor of the trapezoidal grooves permits an undistorted visibility through the transparent riblet film which is essential for crack inspection on aircraft.

1. Introduction

Drag reduction research is usually motivated by exciting expectations. In most cases, however, if the research is not contaminated by wishful thinking, the results are rather modest or downright disappointing. Thus, the process of achieving something useful is rather cumbersome and time-consuming. Nevertheless, we shall not dwell here on all the difficulties and failures that we have encountered, but, rather, we shall outline in brief the essential ideas and findings of our research. In addition, we shall deal here only with two drag reduction concepts: *riblet surfaces* and *slit surfaces*. We combine the description of our investigations on these two aspects because our test hardware was designed for both purposes.

1.1. *Riblet surfaces*

The fact that ribbed surfaces (riblets) aligned in the streamwise direction do reduce turbulent skin friction has been established beyond any reasonable doubt. There are a large number of independent measurements available from many laboratories (e.g. Walsh 1980, 1982, 1983; Nitschke 1983; Walsh & Lindemann 1984; Bechert, Hoppe & Reif 1985; van Dam 1986; Choi 1987; Sawyer & Winter 1987; McLean, George-Falvy & Sullivan 1987; Dinkelacker, Nitschke-Kowsky & Reif 1988; Wilkinson & Lazos 1988; Walsh, Sellers & McGinley 1989; Rohr, Anderson & Reidy 1989; Neumann & Dinkelacker 1989; Nieuwstadt *et al.* 1989; Coustols & Cousteix 1990; van der Hoeven & Bechert 1991. An excellent survey has been compiled by Walsh 1990). These data have been collected by various direct measurements with shear stress balances, with pressure loss measurements in tubes and in aircraft flight experiments. In most cases, sawtooth riblets with a triangular cross-section (Walsh 1980) have been used. Our own measurements with this configuration produced 5.1% turbulent shear-stress reduction. Thus, our aim has been to achieve a greater drag reduction.

The mechanism of this drag reduction, however, was not well understood until recently. The first hypothesis on drag reducing surfaces (Kramer 1939) was that these surfaces would redistribute the shear stress, with a high concentration at the protruding parts of the surface. This is obviously so (Granola, Murcsy-Milian & Tamasch 1991), but it does not provide a satisfactory explanation of why these surfaces do reduce drag. A more plausible explanation is that longitudinal ribs rectify the turbulent flow in the mean-flow direction by hampering the fluctuating cross-flow component w'. If the w'

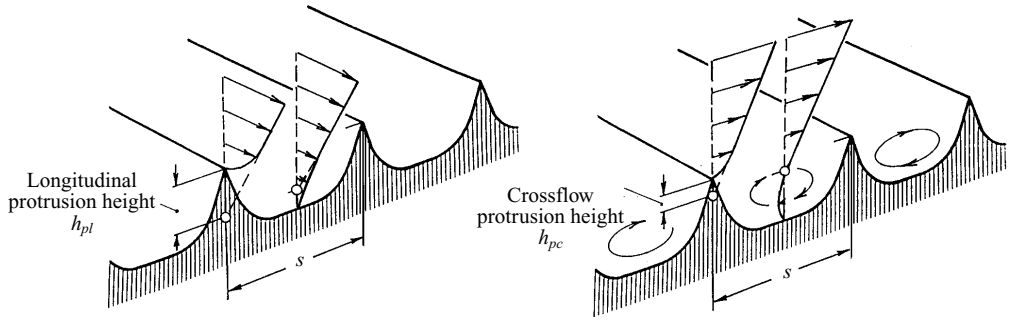

FIGURE 1. Viscous longitudinal and crossflow on a ribbed surface. $\Delta h = h_{pl} - h_{pc}$.

fluctuations close to the surface can be reduced, the turbulent momentum transfer close to the surface will also be reduced and, consequently, the shear stress will be decreased. This mechanism has been suggested by us previously (Bechert *et al.* 1986; Bechert & Bartenwerfer 1989). Our previous calculations were based on the assumption that the riblets are immersed in the viscous sublayer of the boundary-layer flow, which is true for the major part of the drag reduction regime of riblets.

However, at that time, we only had calculations of the longitudinal flow on ribbed surfaces available. We felt that the 'protrusion height' h_{pl} of the longitudinal flow (see figure 1) had some importance pertaining to drag reduction. The protrusion height is the distance between rib tip and (average) origin of the velocity profile near the surface. However, this suggestion, albeit almost correct, is not completely convincing. For instance, a surface with spikes, in an arrangement without preferred orientation, can have a considerable protrusion height without any rectifying or drag reducing effect.

Thus, being worried about this inconsistency, we have shown in our IUTAM paper (Bechert, Bartenwerfer & Hoppe 1990) that longitudinal and crossflow have to be considered. The important finding of this paper was that even in the viscous flow limit, there is a significant difference between longitudinal and crossflows. Whereas the longitudinal flow is obviously always attached, the crossflow separates between the ribs, even in the viscous flow limit (our attention has been drawn to this fact by R. L. Panton (private communication, 1988).). Recently, this fact has been confirmed analytically by Luchini, Manzo & Pozzi (1992). For a viscous Couette flow above a single cavity, this observation had been made previously (Takematsu 1966; Taneda 1979; Higdon 1985).

More important, however, is the fact that the origin of the crossflow differs in its location from the origin of the longitudinal flow (see figure 1). In our IUTAM paper, we have determined the origin of the viscous crossflow by a plate-bending analogy experiment. Subsequently and independently, Luchini, Manzo & Pozzi (1991) calculated the viscous crossflow on various ribbed surfaces. They found that the maximum possible difference Δh between the heights of the two origins (see also figure 1) is $\Delta h = 0.132s$, where s is the lateral rib spacing. This maximum value of Δh occurs for very sharp and thin ribs (blade riblets) and deep grooves. If a three-dimensional flow perturbation occurs at a certain height y above the surface, then the shear stresses in the streamwise and in the crossflow directions will be different. Since the origin of the crossflow is closer to the rib tip, the shear stress of the crossflow is increased. Owing to this higher crossflow resistance, the crossflow fluctuations w' are reduced. This expected w' decrease was confirmed by numerical Navier–Stokes computations (Choi,

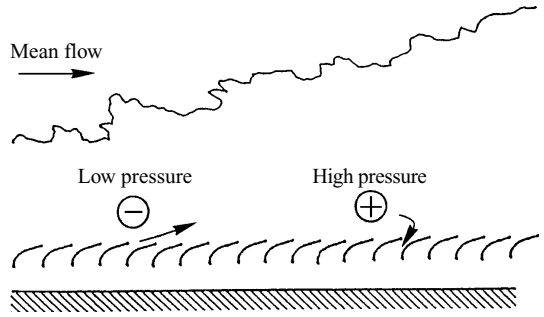

FIGURE 2. A schematic of the 'slit ejection mechanism'.

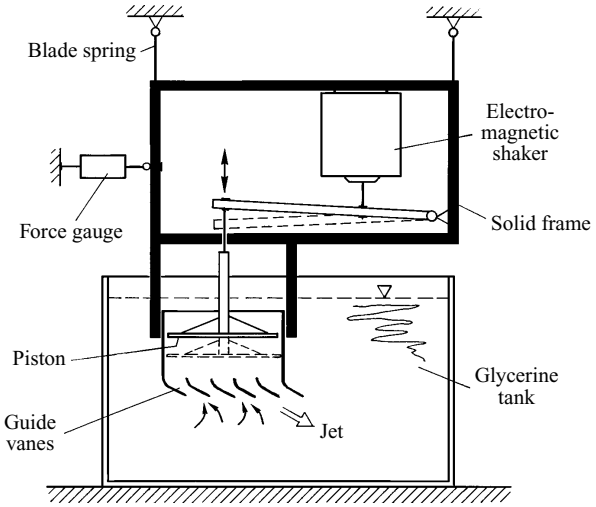

FIGURE 3. Glycerine tank experiment with pulsating slit flow.

Moin & Kim 1993) and experimentally by Weiss (1993) and by Suzuki & Kasagi (1994). In a more specific numerical investigation on this issue, Goldstein, Handler & Sirovich (1995) also conclude that hampering of crossflow fluctuations is the mechanism of riblet drag reduction. Finally, our concept is supported by the fact that drag reduction, in particular at low Reynolds numbers s^+, seems to be proportional to $\Delta h/s$. This supposition will also be evident from the data of the present paper.

1.2. *Slit surfaces*

In previous papers (Bechert *et al.* 1985, 1990) we have suggested a hypothetical 'slit ejection mechanism'. The idea was to have a surface as shown in figure 2. The basic concept is this: the fluctuating pressures in a turbulent boundary-layer flow drive the fluid into and out of small slits in a surface. The slits in the surface are connected by a cavity underneath. The pressure in this cavity is the same as the mean flow static pressure (or perhaps slightly lower). The flow into the slits is a sink flow whereas the outflow is a jet flow in the streamwise direction. During the outflow phase, thrust is generated which is assumed to produce drag reduction. Obviously, the slits have to be small, their dimensions being similar to those of riblets. A crucial question was whether or not this mechanism would work at the expected low Reynolds numbers. Independent model experiments with an artificially forced unsteady glycerine flow (Bechert & Hoppe 1988) demonstrated that this thrust effect still worked at $Re_s \approx 10$, albeit with

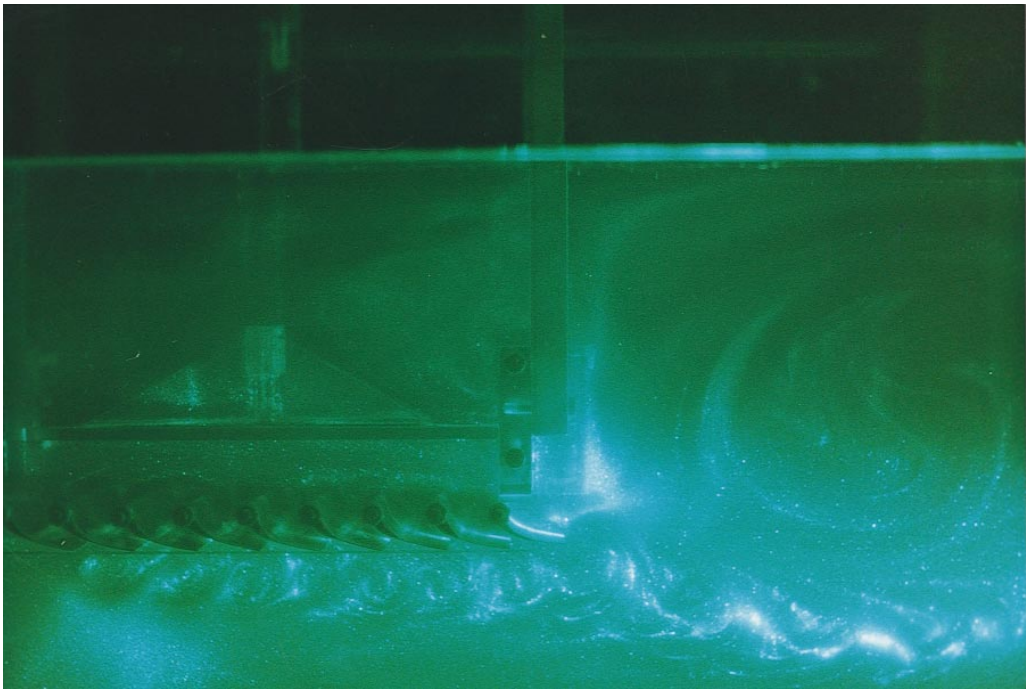

FIGURE 4. Steady jet flow pattern produced by the pulsatile flow through the slits.

low efficiency. In this case, The Reynolds number Re_s was calculated with the average flow velocity in the slits and with the slit width. In addition, the frequencies of the unsteadiness of the flow in the boundary layer were not expected to reduce the thrust significantly. On the other hand, the hypothesized effect could be large because the driving force, i.e. the r.m.s. value of the pressure fluctuations in a turbulent boundary layer, is about three times greater than the average shear stress τ_0 (Blake 1986). Thus, our previous estimations of the drag reduction potential of slits looked quite exciting.

In order to illustrate our previous glycerine tank experiments (Bechert & Hoppe 1988), we show our test arrangement in figure 3. A rectangular piston is driven by an electromagnetic shaker. The piston produces a pulsatile flow in a row of guide vanes. In this simplified model experiment, there is no mean flow with a boundary layer as in figure 2, but the pulsatile flow is discharged into a fluid at rest. The steady thrust generated by the pulsatile glycerine flow can be measured by a force gauge. As can be seen in the flow visualization of figure 4, a steady jet flow to the right-hand side is generated. Actually, the jet flow in figure 4 consists of a row of vortices. When fluid is expelled by the piston, vorticity is shed as sheets of finite length at the trailing edges of the guide vanes. These finite sheets roll up into vortices which are propelled by their own induction and hence a jet is formed. The flow structure is made visible by aluminium flakes in the glycerine. Actually, it is a glycerine-water mixture with a very small amount of water. Its viscosity is $\nu = 10^{-4}\ \mathrm{m^2\,s^{-1}}$, i.e. one hundred times more viscous than water. In this particular experiment, the frequency is 1 Hz and the peak value of the fluctuating velocity in the guide vane slits is $18.8\ \mathrm{cm\,s^{-1}}$. The slit width is 4 mm. Hence, the peak Reynolds number is $Re_s = 7.52$. The Strouhal number is very low, i.e. 0.021.

This previous pilot experiment, albeit impressive, does not provide *per se* any evidence as to whether or not a surface with slits may indeed produce drag reduction

when exposed to a real turbulent flow. For instance, we have no way to estimate the turbulent momentum transfer on such a surface, which certainly plays a role here. Therefore, in the present investigation, a 'full scale' experiment with a slit surface is set up in our oil channel.

2. Test facility

The basic configuration of our oil channel can be seen in figure 5. It has a rectangular cross-section of 25 cm × 85 cm, and it is filled with 4.5 metric tons of baby oil. We have previously given a fairly detailed description of this facility (Bechert *et al.* 1992).

The channel is operated at turbulent flow conditions. The channel Reynolds number Re_{ch}, calculated with the average velocity and the lateral channel width (25 cm), can be varied between $Re_{ch} \approx 5000$ and $Re_{ch} \approx 33000$. The adjustable turbulators (see figure 5) are set so that the mean-flow velocity profile in the channel is symmetrical and does not vary between 5 m upstream of the test section and the test section itself. Nevertheless, even a misadjustment of the turbulators does not perceivably change the data (see Bechert *et al.* 1992). On the other hand, the channel Reynolds number has a weak influence on the data. In particular below $Re_{ch} \approx 10000$ our drag reduction data deviate more and more from previous high-Reynolds-number data. This is a trend which may be expected from Wei & Willmarth's (1989) measurements of turbulent channel flow. They show that turbulence data are not uniform below about $Re_{ch} \approx 10000$. Thus, the data published here was collected only between $Re_{ch} = 10000$ and $Re_{ch} = 33000$.

Deviating from previous oil channels, the Berlin oil channel has a very accurate shear-stress balance. It operates with direct force measurements on rectangular test plates (400 mm height and 500 mm length in the streamwise direction) which are inserted into the sidewalls of the channel. The high accuracy is obtained by directly comparing the shear force of a ribbed test plate to that of a smooth reference plate, which is inserted into the opposing channel wall. In this way, the accuracy is enhanced significantly. It is $\pm 0.3\%$ of the measured shear stress. This accuracy includes errors due to misalignment of the plates in the channel. However, in a test series with a plate having variable geometry which is not removed between tests, the accuracy is even better. In this situation, the reproducibility is limited by the precision of the mechanical gear system with which the individual surface configuration is adjusted (± 0.1 mm) and by the limited integration time (5–20 minutes) of the measurement.

Obviously, even for smooth surfaces, the turbulent shear stresses on both sides of the channel are not exactly identical. The deviations, which are of the order of one per cent, can be almost completely eliminated by a fine adjustment of the turbulators upstream of the test section (see figure 5). The residual shear-stress difference is very small, having a value between 0 and 0.6% over the measuring range. This difference has been subtracted in our data processing. (In our previously published data (Bruse *et al.* 1993) this difference was not taken into account. By including this correction, the weak apparent Reynolds-number dependence of the data which had been suggested there, vanishes.)

It should be mentioned that the present measurements were carried out with zero pressure gradient. This condition is achieved with a movable lid on top of the test section (see Bechert *et al.* 1992). The position of this lid is adjusted for each Reynolds number individually. This adjustment procedure is discussed in Appendix B. The experimental conditions of the oil channel are listed in table 1. In the first column, we

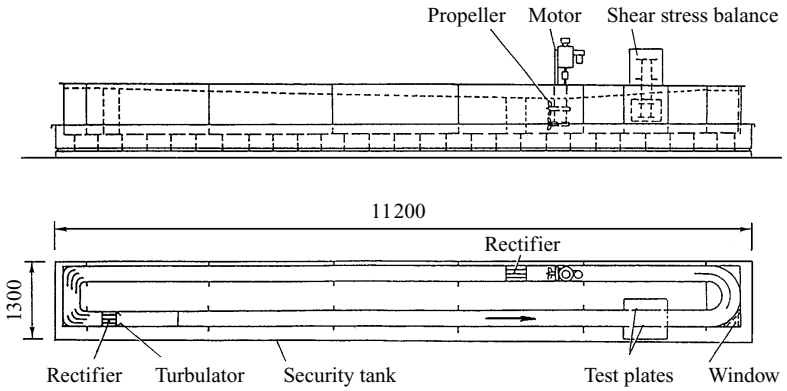

FIGURE 5. Schematic of the Berlin oil channel. Dimensions in mm.

Drive shaft speed (r.p.m.)	Average velocity $\bar{u}$ between test plates (m s^{-1})	Reynolds number of the channel Re_{ch}	Wall shear stress τ_0 (N m^{-2})	$c_f \times 10^3$ measured	$c_f \times 10^3$ predicted
300	0.395	8224	0.481	7.38	7.50
400	0.558	11632	0.910	7.00	6.88
500	0.731	15220	1.447	6.49	6.43
600	0.910	18960	2.103	6.08	6.09
700	1.096	22830	2.878	5.74	5.81
800	1.287	26816	3.769	5.45	5.59

TABLE 1. Typical data on the turbulent shear stress and its dependence on the channel operation parameters

have given the drive shaft speed of the channel which, admittedly, has no general significance, but helps to identify data. A typical shear stress data set consists of 12 data points with data taken between 322 r.p.m. and 850 r.p.m. at shaft speed increments of 48 r.p.m. As a reference velocity we use the average velocity $\bar{u}$ between the test plates where the channel flow is nearly two-dimensional (see also our paper on the oil channel, Bechert *et al.* 1992). The Reynolds number of the channel Re_{ch} is calculated with this velocity and with the horizontal channel width, i.e. 25 cm. The kinematic viscosity is typically $\nu = 1.20 \times 10^{-5}$ m^2 s^{-1}. (The variation of viscosity with oil temperature is not neglected in our measurements.) In addition, we provide here the wall shear stress τ_0 as measured on the (smooth) test plates with our mechanical balance. The measured wall-friction coefficient c_f,

$$c_f = \frac{\tau_0}{\frac{1}{2}\rho\bar{u}^2}, \tag{1}$$

is also given in table 1. This friction coefficient can be predicted theoretically. In textbooks of fluid mechanics (see e.g. Schlichting 1979) we find Blasius' law for the friction coefficient c_f (based on the average velocity $\bar{u}$) in a turbulent pipe flow given by

$$c_f = 0.0791 \left(\frac{\bar{u}d}{\nu}\right)^{-1/4}, \tag{2}$$

with d being the diameter of the tube. For an extension to a non-circular cross-section such as ours, one usually assumes (Schlichting 1979, p. 612) an equivalent 'hydraulic diameter'

$$d = \frac{4a}{c}, \tag{3}$$

where a is the cross-sectional area and c is the wetted perimeter. For our rectangular channel with a flow cross-section of $25 \times 75\,\mathrm{cm}^2$ we find $d = 37.5\,\mathrm{cm}$. With this equivalent diameter we have calculated the values for c_f in the last column of table 1. The good agreement with our measurements is surprising and probably somewhat fortuitous, but it demonstrates at least that our flow is a fully established turbulent channel flow without any unusual properties. This fully turbulent channel-flow situation has been achieved by a proper turbulator setting so that over a long distance (5 m) upstream of the test section the flow exhibits identical mean flow profiles.

In previous investigations, the shear stress distribution on the test surfaces has not been measured. Usually, the shear stress distribution exhibits much larger variations than the mean flow velocity distribution does. As has been demonstrated in our description of the test facility (Bechert *et al.* 1992), the velocity distribution is quite even. In order to ascertain the quality of the present experiments, we have also measured the shear stress distribution with a Preston tube, using a new and simplified calibration procedure (Bechert 1996). The shape of the shear-stress distribution and its influence on our data is discussed in Appendix A.

Another item of concern is secondary flow in the test section. Obviously, the turbulent flow in a rectangular channel does produce secondary flows. On the test plates, however, it turns out that they are very weak. We have investigated this with a small device near the wall; the device was similar to a wind vane (with zero buoyancy in the oil). The deviations in mean flow direction were always below 5° on the test plates. The weak secondary flow was directed towards the middle of the plate where the higher shear stress occurred. From previous investigations on the crossflow effect on riblet surfaces (Bechert, Gerich & Hoppe 1987; Walsh 1990) we know that a crossflow angle of less than about 10° has no detectable effect on riblet drag reduction. Hot-film measurements in the oil channel are currently underway, and we shall report on these results separately.

More important, however, than the assertion that the flow quality is suitable, is a direct comparison with previous data on ribbed surfaces obtained in wind tunnels. The following section will deal with this comparison.

3. Connection with previous data: triangular and scalloped riblets

For a comparison of our oil-channel data with previous wind-tunnel results, we started our investigation with a verification of measurements with sawtooth riblets with 60° ridge angle, similar to the ones tested by Walsh (1980, 1982). Walsh had a 54° ridge angle in his riblet geometry where the riblet height equalled the lateral spacing. In our oil channel measurements we collected data with $\alpha = 60°$ ridge angle and with two different lateral rib spacings: 3.04 and 6.1 mm. In figure 6, we show the comparison of these data with previous wind-tunnel data by Walsh and ourselves.

In figure 6 the Reynolds number for the riblets s^+ is defined as usual, namely,

$$s^+ = \frac{su_\tau}{\nu}, \tag{4}$$

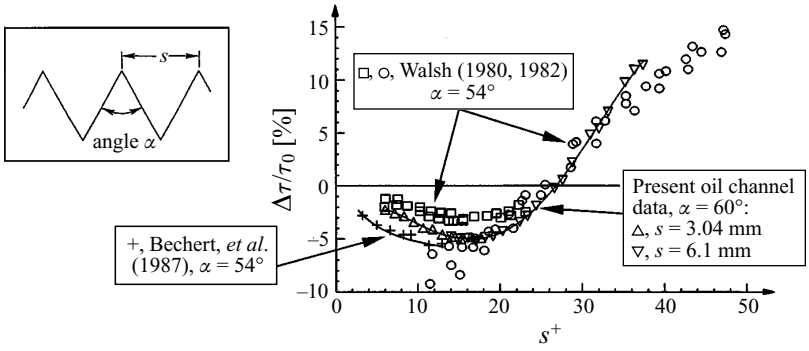

FIGURE 6. Measurements with sawtooth riblets.

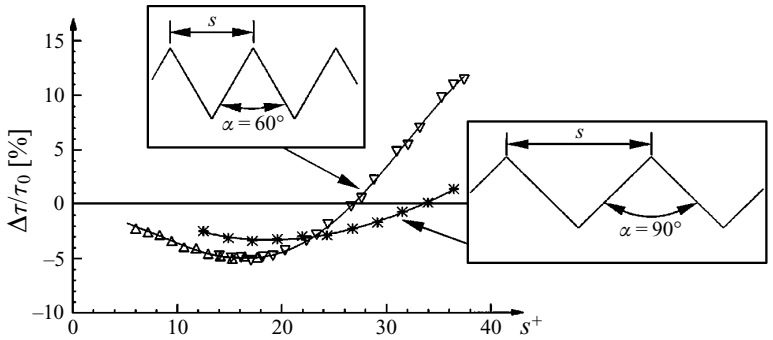

FIGURE 7. Sawtooth riblets with different ridge angles.

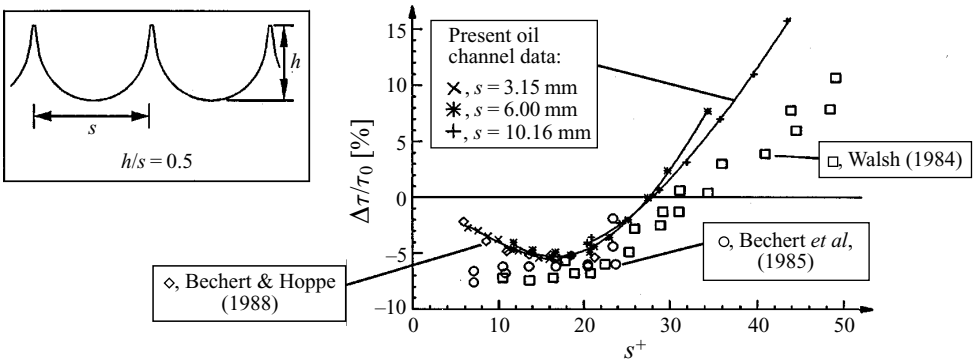

FIGURE 8. Measurements with semi-circular scalloped riblets.

with s being the lateral rib spacing. The velocity u_τ is defined as before, $u_\tau = (\tau_0/\rho)^{1/2}$, with τ_0 being the shear stress on the reference plate exposed to identical flow conditions. $\Delta\tau$ is the difference of the shear stresses between test plate and smooth reference plate, $\Delta\tau = \tau - \tau_0$. Negative values of $\Delta\tau/\tau_0$ correspond to drag reduction, and positive values to an increased drag.

As it turns out, figure 6 illustrates the accuracy of different measurements rather than enabling subtle statements on compatibility to be made. However, within the error bars of previous measurements, compatibility is reasonably confirmed. In order to show that a change in angle from 54° to 60° (the latter is easier to handle both theoretically

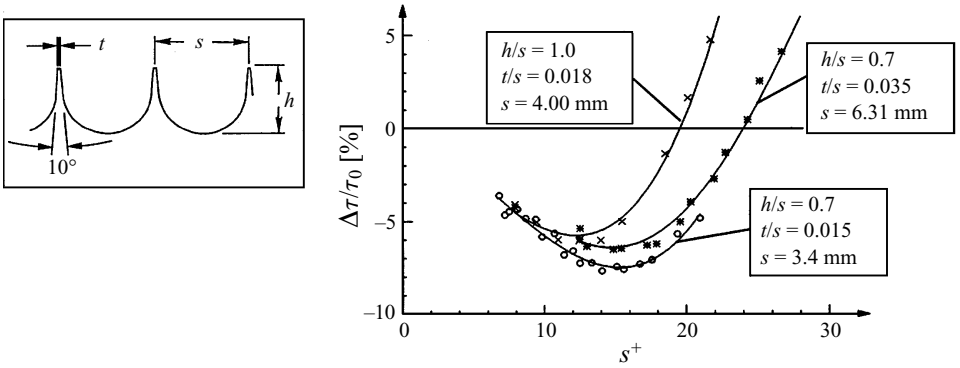

FIGURE 9. Scalloped riblets with increased groove depth.

and in terms of available milling tools) is probably not so important, figure 7 gives data with ridge angles of $\alpha = 60°$ and 90°.

Another check with previous data can be seen in figure 8. There, data are shown which were collected with scalloped riblets having semicircular cross-section. Again, we compare our present oil-channel measurements with previous ones obtained in wind tunnels. The comparison again looks reasonable if one keeps in mind that the wind-tunnel data are less accurate.

As a first step away from previous data, we tried to enhance the performance of scalloped riblets by increasing the groove depth (see figure 9). These surfaces, and those used in figures 6–8, have been milled in Plexiglas. With this production technique, a continuous variation of the groove depth was not possible. However, the data of figure 9 suggest that the optimum is located near $h/s = 0.7$. For a better understanding of the data in figure 9, it should be mentioned that even for the oil channel with its large rib dimensions, the manufacture of nominally identical geometry but with differing size still poses a challenge. In particular, the data with $h/s = 0.7$ show a different ridge width t/s and thus a different drag reduction. This demonstrates the paramount importance of the rib-tip sharpness for drag reduction.

Another fact is clearly visible in figure 9: the low s^+ regime of the curves with $h/s = 0.7$ and $h/s = 1.0$ is identical. The curve with $h/s = 1.0$, however, turns away from the common tangent and eventually ascends with a steep slope. On the other hand, the $h/s = 0.5$ curve in figure 8 exhibits a much flatter shape, even at low s^+. In the following sections of this paper, this particular behaviour will be worked out more clearly.

4. Experiments with slits and ribs

In order to investigate the suggested drag reduction by the 'slit ejection mechanism' we have designed a test plate which contains slits with variable geometry. It appeared meaningful to combine this with longitudinal blade ribs to be able to also investigate the combined effect. On the other hand, our test plate enables us to study both effects separately: (i) slits alone by elevating the slit structure above the rib structure and (ii) blade ribs alone by closing the slits. A schematic of our test plate can be seen in figure 10.

The lateral rib spacing is $s = 5$ mm. For the ribs we use 75 longitudinal blades which are attached to a very rigid frame. These blades are placed under tension with 300 N force each in order to obtain 'rigid' conditions or, in other words, to avoid fluid–elastic interactions. The 2590 slits are directed in the downstream direction, and their width

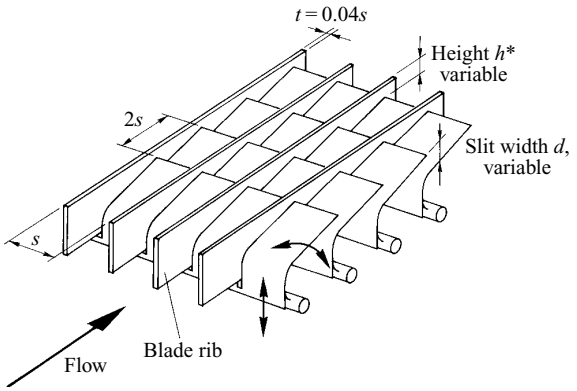

FIGURE 10. Adjustable surface with slits and longitudinal ribs. $h = h^* + d$.

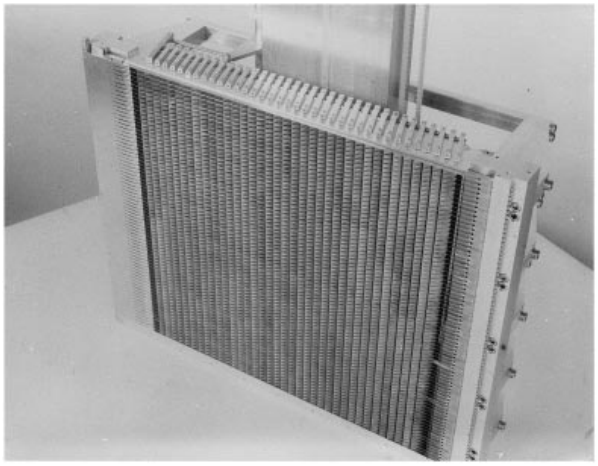

FIGURE 11. Photograph of test plate with slits and longitudinal ribs.

d can be changed simultaneously by an array of levers. In addition, the whole guide-vane system with the slits can be varied in its elevation h relative to the longitudinal blades (see figure 10). Both slit width and elevation adjustment can be changed during the running of an experiment without disassembling any parts and without recalibration. Figure 11 shows the test plate. On the right-hand side of the plate, part of the sheet-metal fairing is removed in order to show the suspension of the longitudinal blades. More detailed information on the technology of the test plate is given in Appendix B. This additional information also pertains to the other test plates being used.

It is interesting to see how a slit surface behaves in a realistic turbulent-flow environment. In figure 12, fans of data with various slit widths d/s and various groove depths h/s are shown. The best data are obtained (7.6 % drag reduction in this case) if the slits are completely closed. On the other hand, if the slits are elevated above the tips of the longitudinal blades, i.e. if the longitudinal blades are absent in terms of fluid dynamics, the shear stress is always increased above that of a smooth plate. By contrast, if the slits are submerged in the grooves, the situation improves somewhat. For instance, if the slits are open with $d/s = 0.2$ (or 10 % porosity) and submerged for optimal shear stress reduction by the ribs (= blades), the rib performance is only 0.9 % worse. This finding may be important for porous surfaces for boundary-layer suction.

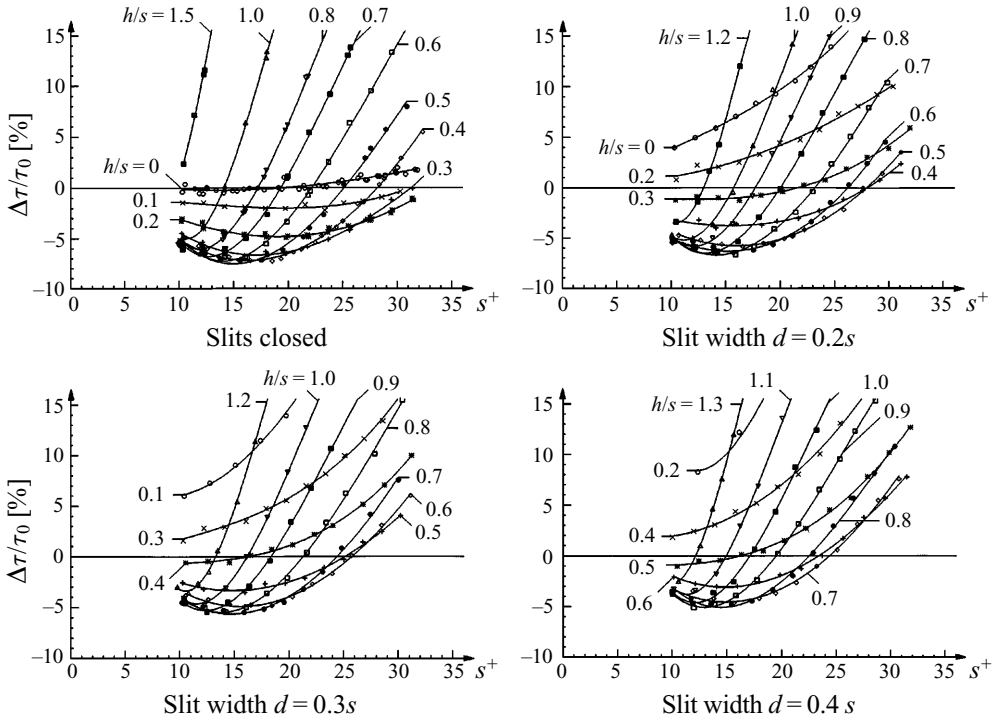

FIGURE 12. Shear stress data of the plate with slits and longitudinal blades.

On the other hand, as can be seen clearly from figure 12, the performance becomes very poor when the slits are wide open.

Thus, it is clear that our suggested 'slit ejection mechanics' does not work as a scheme for turbulent wall shear stress reduction. Our arguments are: the fluctuating flow through the surface enhances the vertical velocity v' near the rib tips and with it the momentum transport which produces the turbulent shear stress $-\rho\overline{u'v'}$. Therefore, any beneficial effect from the slits is overwhelmed by the deleterious effects of an enhanced turbulent shear stress.

At this point, however, we have to mention that the present verdict on porous surfaces cannot be generalized to all conceivable passive surfaces. In our experiments, we have had only one type of surface impedance, i.e. positive pressure corresponding to a local flow through the surface (negative v'), with both quantities being basically in anti-phase, provided that the Strouhal number of the slit is low, which means that the inertia of the flow through the slit does not matter. The latter can be assumed to be essentially valid for our experiments. However, one cannot exclude that with other types of wall impedances a different behaviour may occur, as has been suggested by Carpenter (1995) for transitional flows. Nevertheless, the present investigation has produced data which strongly suggest that all 'normal' leaks and porosities have a deleterious effect in turbulent flows on a wall.

5. Optimization of blade riblets

In figure 12, it is particularly interesting to see the data with closed slits. This data is, in fact, an optimization of blade riblets with variable groove depth. In figure 12 we have a blade thickness of $t/s = 0.04$ which produces 7.6 % drag reduction. We expect

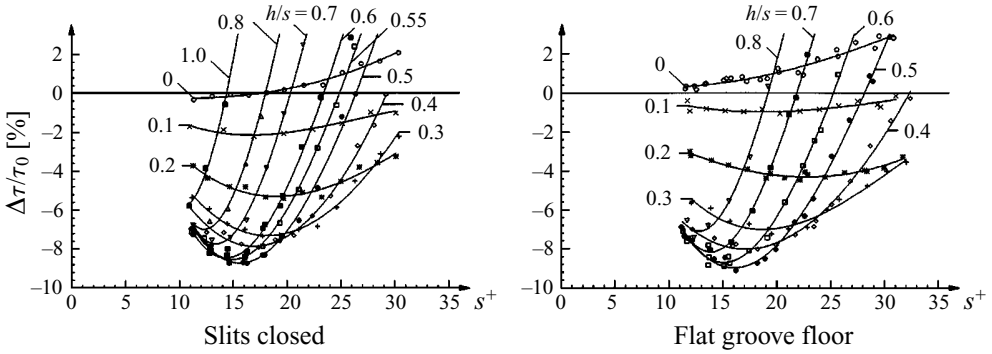

FIGURE 13. Optimization of blade riblets, decreased blade thickness $t = 0.01s$.

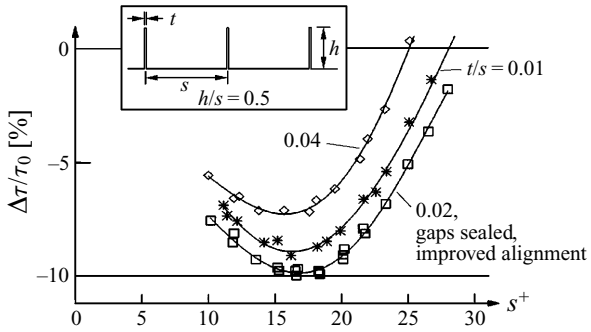

FIGURE 14. Optimal blade riblets. Elimination of deleterious effects.

a significant improvement for thinner blades because we assume here that $\Delta h/s$ has a higher value, according to the viscous theory (Bechert & Bartenwerfer 1989; Luchini *et al.* 1991). Therefore, we also tested thinner blades with $t/s = 0.01$.

A comparison between figures 12 and 13 clearly shows that there is an improvement from 7.6% to 8.7% drag reduction. Our slit/blade-rib surface had small steps (step height $0.05s$) on the groove floor when the slits were closed. When this groove floor was replaced by a flat groove floor (technological details: see Appendix B, figure 27), the data were only marginally improved to 9.0% (see figure 13). Nevertheless, the optimal groove depth is determined from figures 12 and 13 to be $h/s = 0.5$.

At $h/s = 0$, our adjustable surfaces should behave like smooth surfaces. However, in our data above $s^+ \approx 20$ there are deviations (see figure 13) towards higher drag, i.e. parasitic effects do occur. These are partly caused by small steps at the leading and trailing edges of the adjustable groove floor (details: see Appendix B, figure 26). At increasing h/s, however, this becomes less important because the steps are then submerged in the grooves. Another deleterious effect consists of residual porosity caused by small longitudinal gaps between the blades and the groove floor. These gaps are necessary because the groove floor has to be moved up and down between the blades during the search for an optimal groove depth. Depending on which test plate has been used, this parasitic porosity can be as large as 5–10%. (Here, we define the porosity as the ratio of the gap width to the lateral groove spacing or, more simply, as the ratio of open to closed surface.) Once we have acknowledged from figure 12 that porosity is, as observed before, a deleterious effect, we expect a slight improvement from sealing these gaps with plastic (oil-resistant) tape. In addition, a good blade alignment is expected to help.

As can be seen in figure 14, the elimination of the above-mentioned deleterious effects does indeed improve the results. The blade height was adjusted to its optimal value $h/s = 0.5s$ and the gaps were sealed. We used our second adjustable surface (see Appendix B) on which the blade height could be more evenly aligned. The only minor drawback was that blades thinner than $t/s = 0.02$ could not be inserted there because of buckling problems. Nevertheless, a record value of 9.9% drag reduction was obtained.

6. On the mechanism of riblet drag reduction

Our concept on how ribbed surfaces reduce drag has already been mentioned in the introduction. It is based on the finding that longitudinal rib structures impede crossflow near the wall, even in the viscous flow limit. This latter situation corresponds to a low Reynolds number s^+, (see figure 15).

The quantity which matters for the hampering effect on the crossflow is the height difference Δh between the origins of longitudinal and crossflows (see figure 1). For a given geometry, Δh is a constant fraction of the lateral rib spacing s. Therefore, with increased s, the difference Δh of the origin heights will also increase. Because the hampering effect on the crossflow is then enhanced, the turbulent crossflow (w') near the surface will decrease and with it momentum exchange and drag. For a basically viscous interaction with the ribs we expect a linear behaviour, and that is what we see in figure 15 for low Reynolds numbers s^+. Actually, since Δh is the relevant quantity, the drag reduction should depend on the Reynolds number Δh^+ rather than on s^+. For practical reasons, however, we retain the plotting of data with the drag reduction $\Delta\tau/\tau_0$ versus s^+. The initial slope of the curves should then be represented by

$$\frac{\Delta\tau}{\tau_0} \propto \frac{\Delta h}{s} s^+. \tag{5}$$

A quantitative connection between the protrusion height difference Δh and the initial slope of the drag reduction curve has been proposed by Luchini (1992). To our knowledge, this approach has not yet appeared in a journal. Therefore, we will show here the basic steps of his theory.

The impeding influence of the riblets on the lateral velocity fluctuation w' is taken into account by assuming that for w' and other properties of the turbulence only the origin of the crossflow (see figure 1) is relevant. Thus, the turbulent flow above the viscous sublayer 'sees' this crossflow origin as its origin. Hence, the thickness of the viscous sublayer is increased by Δh, the difference between the heights of the origins of longitudinal and crossflows. An increased thickness of the viscous sublayer corresponds to a drag reduction, as will be shown in detail.

In the following calculations, we non-dimensionalize the velocities with u_τ, namely, $u^+ = u/u_\tau$. Lengths like the distance y perpendicular to the wall are normalized as $y^+ = yu_\tau/\nu$. A turbulent velocity profile on a smooth wall takes the form $u^+ = y^+$ in the viscous sublayer close to the wall. In the logarithmic regime above it we have $u^+ = 2.5 \ln y^+ + A$, with $A = 5.5$ (see e.g. Schlichting 1979). We take as the origin of the logarithmic regime the point y_0^+ where the two velocity laws meet, determined by

$$y_0^+ = 2.5 \ln y_0^+ + A. \tag{6}$$

From equation (6) we find $y_0^+ = 11.635$. Now we assume, as indicated above, that y_0^+ increases by Δh^+. By this growth in sublayer thickness, the logarithmic region has to move upwards and the constant A has to assume a higher value (this type of behaviour

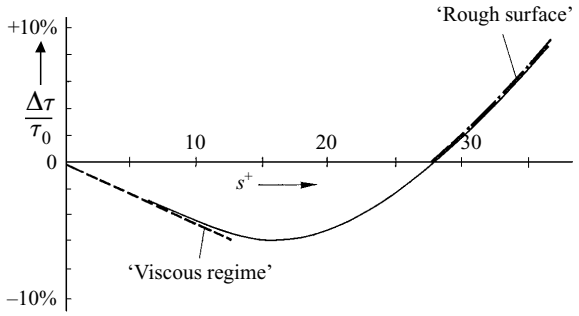

FIGURE 15. General structure of a drag reduction curve.

is also found in polymer drag reduction in liquids). By linearizing (6) around the values of smooth surfaces and letting $y_0^+ = 11.635 + \Delta h^+$, we find, for small deviations of A,

$$A = 5.5 + 0.785\Delta h^+, \tag{7}$$

where $\Delta h^+ = \Delta h u_\tau/\nu$. Now we have to find out how a change in A translates into a change of the wall friction coefficient c_f (or the shear stress τ). As we have seen, our channel flow bears some resemblance to a pipe flow. In particular because in a channel, an average velocity $\bar{u}$ is meaningful, and not a free-stream potential flow velocity u_∞, which actually does not exist. (As Luchini (1992) has shown, however, the final equation (10) is the same for the turbulent flow above a flat plate. It should also be mentioned, that in our equations the numerical coefficients deviate minimally from Luchini's, because our boundary-layer data are based on the semi-empirical data in Schlichting (1979).)

Prandtl's universal law of friction for a smooth pipe can be written in the following form (Schlichting 1979, pp. 609–611):

$$\frac{1}{(c_f/2)^{1/2}} = 2.5\ln\left(\frac{\bar{u}d}{2\nu}(\tfrac{1}{2}c_f)^{1/2}\right) + A - 3.75. \tag{8}$$

In this equation, c_f is, as in table 1, the friction coefficient $c_f = \tau_0/(\frac{1}{2}\rho\bar{u}^2)$ based on the average velocity in the channel $\bar{u}$. This equation can be expanded for small changes in c_f and in A. We find

$$\frac{\delta c_f}{c_f} = \frac{\delta A}{(2c_f)^{-1/2} + 1.25} = \frac{\Delta\tau}{\tau_0}. \tag{9}$$

Using equation (7) we obtain

$$\frac{\Delta\tau}{\tau_0} = \frac{0.785\Delta h^+}{(2c_f)^{-1/2} + 1.25}. \tag{10}$$

Utilizing the friction values c_f in table 1 we find for the lower and the higher channel Reynolds numbers slightly deviating coefficients

$$\frac{\Delta\tau}{\tau_0} = \begin{cases} 0.0809\Delta h^+ & \text{at } Re_{ch} = 11\,632 \\ 0.0725\Delta h^+ & \text{at } Re_{ch} = 26\,816. \end{cases} \tag{11}$$

In order to proceed further, we now need quantitative values for $\Delta h = h_{pl} - h_{pc}$. The longitudinal protrusion height h_{pl} and the crossflow protrusion height h_{pc} have been calculated previously for a number of riblet configurations (see figure 16).

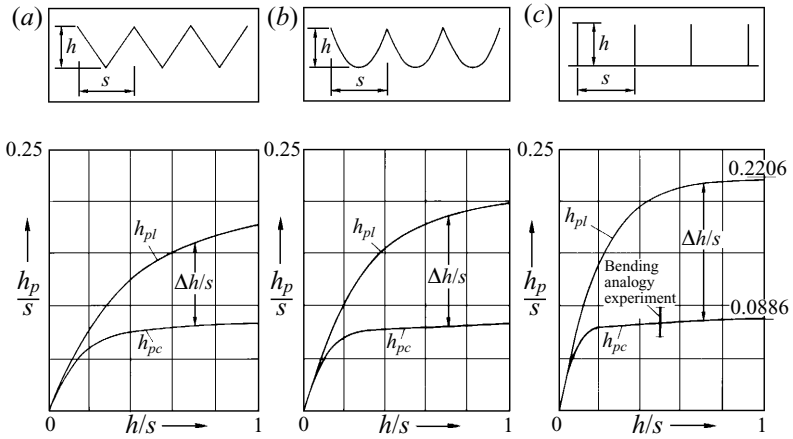

FIGURE 16. Longitudinal flow (h_{pl}) and crossflow (h_{pc}) protrusion heights for ribs with (*a*) triangular, (*b*) parabolic and (*c*) blade shape.

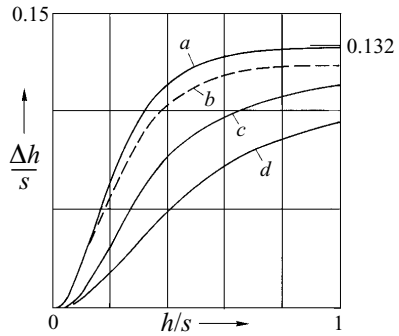

FIGURE 17. Protrusion-height differences for various riblet configurations: (*a*) blade riblets, infinitely thin, (*b*) blade riblets, blade thickness 2% of lateral rib spacing, (*c*) parabolic groove profile, (*d*) triangular riblets.

The data in figure 16 are taken from the work of Bechert & Bartenwerfer (1989) and of Luchini *et al.* (1991). The curve for h_{pc} for blade ribs in figure 16 has been calculated for the present paper by P. Luchini and A. Pozzi (private communication, 1996). Our own previous experimental data on h_{pc} obtained by a plate-bending analogy experiment (Bechert *et al.* 1990) are also shown in figure 16. The relevant quantity Δh for the three configurations can then be seen in figure 17.

The deleterious effect of the finite thickness of the blades in figure 17 has been estimated with an approximate equation developed by Bechert & Bartenwerfer (1989) (see equation (21) there). For this latter correction, only the more significant influence of finite blade thickness on h_{pl} has been taken into account. Having available in figure 17 the value of $\Delta h/s$ for various configurations, we may use equation (10) in a slightly modified form:

$$\frac{\Delta\tau}{\tau_0} = \frac{0.785(\Delta h/s)\,s^+}{(2c_f)^{-1/2}+1.25}. \tag{12}$$

As can be seen in figure 18, Luchini's (1992) prediction for the initial slope of the drag reduction curve is not far off the data. It should be mentioned here that this prediction does not contain any adjusted constants. The predicted initial slope is good

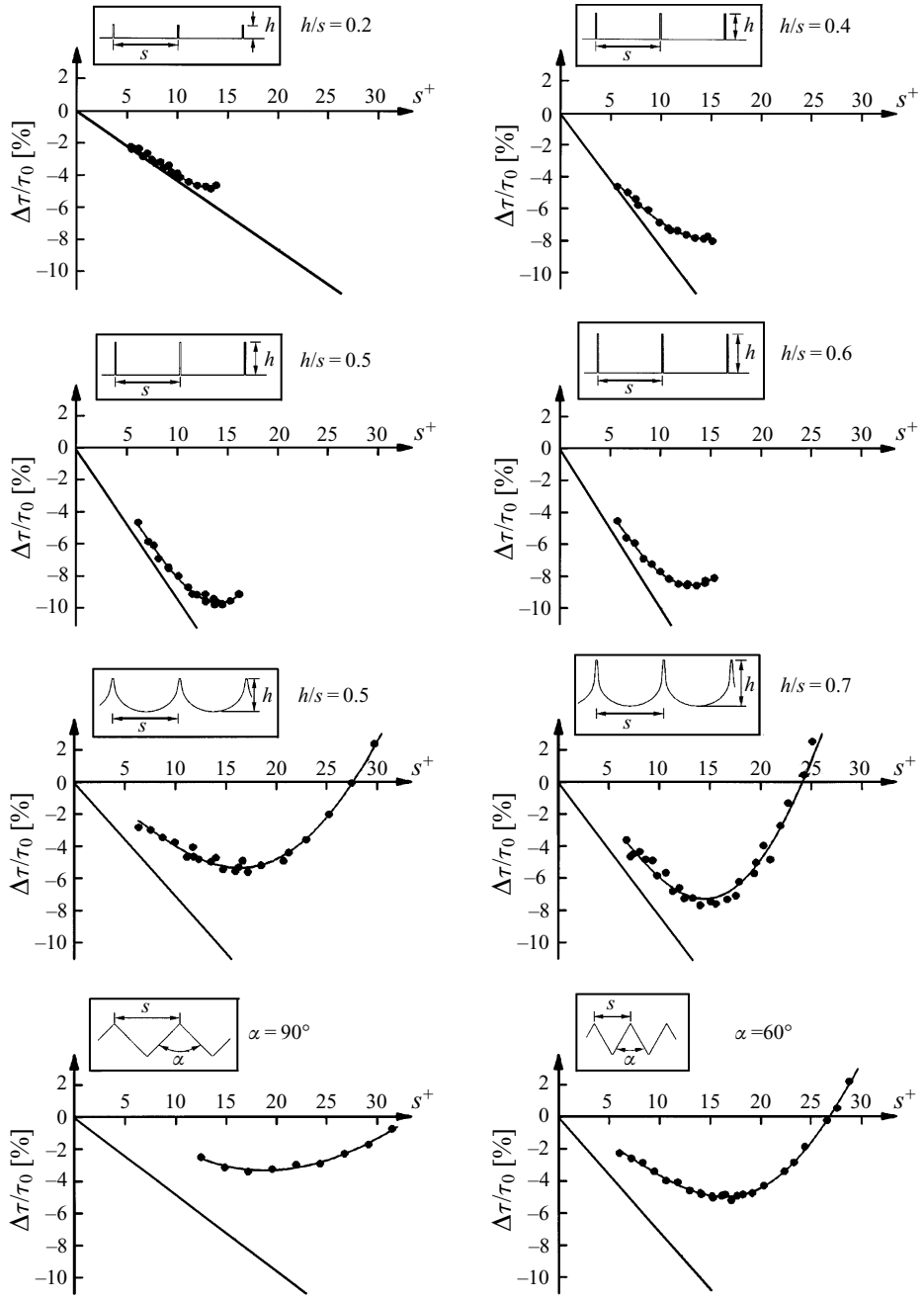

FIGURE 18. The diagonal line is the predicted initial slope of the drag reduction curves (equation (12)) compared with ●, measured data. Only for blade riblets (upper half of figure) the rib tip thickness has been taken into account for the determination of the initial slope with equation (12).

for the blade riblets where the finite thickness of the blades, and thus the sharpness of the ribs, has been taken into account. For both the scalloped and triangular riblets where the finite width of the rib tips has not been considered, the initial slope is overpredicted. Nevertheless, the comparison with the blade riblet data in particular shows that the essential trends are covered by Luchini's asymptotic theory, which

quantitatively relates $\Delta h/s$ with the low s^+ regime of the drag reduction curve. In our research, we had anticipated this relation quite early on, and it turned out to be a useful guideline for our experiments. Following the idea that a high $\Delta h/s$ would lead to high drag reduction enabled us to avoid testing all the riblet configurations which are conceivable.

However, optimizing for high $\Delta h/s$ is not exactly the same as optimizing for the highest possible drag reduction. This is because the initial slope of a curve is not identical with the minimum of that same curve.

Why then do the drag reduction curves deviate from this initial linear behaviour? Obviously, at higher Reynolds numbers s^+, the viscous flow assumptions are no longer valid. Whereas an increase in wetted surface is irrelevant in a viscous Couette flow, it does indeed matter for a turbulent flow at high Reynolds number. Then, the ribbed surface behaves as a rough surface (see figure 15). Very markedly, with deeper grooves (see figure 13) the curves deviate at lower and lower s^+ from the viscous linear regime. We assume that this is caused by sloshing in the grooves. The sloshing is produced by the turbulent pressure fluctuations above the surface. Sloshing causes higher v' fluctuations and, consequently, the turbulent momentum transfer is enhanced, and with it the shear stress is increased. A porous surface with slits also admits more vertical (v') flow and has the same effect (see figure 12). On the other hand, it is plausible that a hard surface located at the floor of the grooves reduces the v' velocity by acting like a mirror. Actually, a mirror image is used in inviscid flow theory to represent a hard surface. A fully viscous flow seems to behave in a somewhat similar way (Higdon 1985, 1990). Thus, it is beneficial to increase the groove depth only up to a point where the saturation of $(\Delta h/s)_{max}$ is nearly achieved. This guarantees a strongly rectifying effect on the crossflow. For groove depths higher than this, say beyond $h/s \approx 0.6$, sloshing becomes more and more important and the performance deteriorates. The limit of sloshing also seems to hint towards blade riblets as possibly the best configuration for a high drag reduction. This is due to the fact that a high $\Delta h/s$ is achieved with a comparatively shallow groove, which keeps the sloshing at bay. The previous viscous calculations did not suggest any other configuration as being better in that sense (see figure 17 and see also Bechert & Bartenwerfer 1989; Luchini *et al.* 1991).

7. Riblets for aircraft

At present, the application of riblets on long-range commercial aircraft appears to be both sensible and most likely. Flight experiments have already been carried out by Boeing and Airbus. However, the riblet configurations that were used in these tests were suboptimal. With this particular aircraft application in mind we now have devised a suitable riblet configuration. It is obvious that the blade riblets of §5 are not useful for this purpose. Thin blade riblets would not be durable and would be difficult to manufacture. Therefore, we devised a riblet geometry which can be produced with conventional plastic rolling or casting processes (see the 3 M patent by Marentic & Morris 1986). A configuration that does not deviate very much from the optimal blade riblet shape is a geometry with trapezoidal grooves and wedgelike ribs. This shape would also allow inspection through the surface, if the plastic material is transparent. Thus, the flat floor would enable optical crack inspection of the aircraft skin under the riblet film. Previous riblet configurations which had been produced for aircraft did not have this property. Actually, this problem has previously inhibited riblet implementation on aircraft.

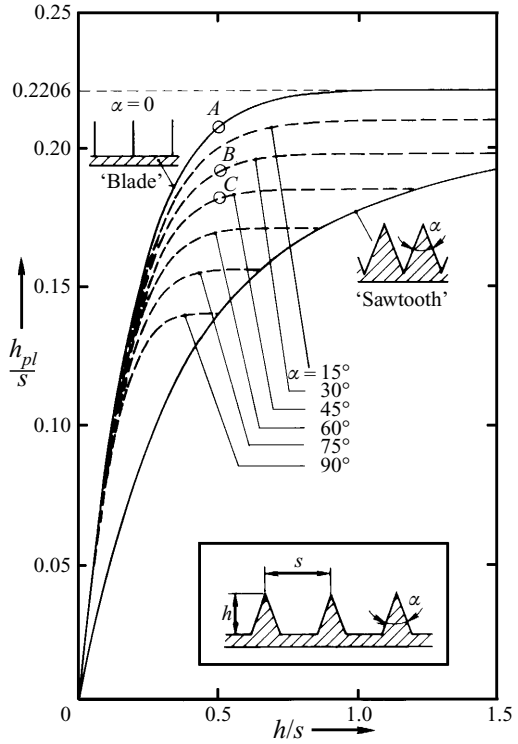

FIGURE 19. Longitudinal protrusion height for ribbed surfaces with trapezoidal grooves.

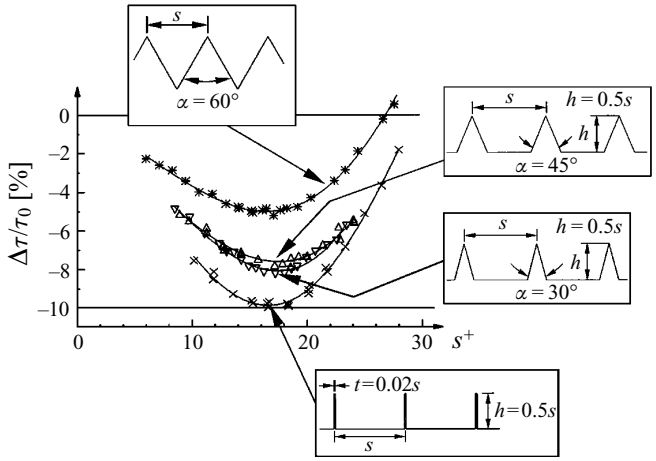

FIGURE 20. Trapezoidal grooves in comparison with other surface geometries.

A suitable design can be selected by looking for a high $\Delta h/s$. Unfortunately, since $\Delta h = h_{pl} - h_{pc}$, this procedure is somewhat hampered by the lack of data for h_{pc}, the crossflow protrusion height. We know, however, from the calculations by Luchini *et al.* (1991) that the location of the crossflow origin remains comparatively close to the rib tip and does not vary very much in its location for $h/s > 0.2$ (see figure 16). Thus we simplify our selection procedure by looking for a high value of the longitudinal protrusion height h_{pl}. This quantity has been calculated previously in sufficient detail

(Bechert & Bartenwerfer 1989). The results can be seen in figure 19. The data in this figure cover the whole scope of conceivable trapezoidal groove configurations. As a groove depth we chose $h/s = 0.5$, the (experimentally determined) optimal value for blade ribs. We see from figure 19 that the more we deviate from the blade riblet configuration with zero ridge angle (case A) the lower h_{pl}/s, and with it $\Delta h/s$, becomes. A decreased $\Delta h/s$ is also tied to a lower drag reduction. Therefore, it is easy to recognize from figure 19 that the wedge angle α of the ribs should be as small as technologically possible. A suitable and technologically feasible wedge angle is, for instance $\alpha = 30°$ (case B in figure 19). Even $\alpha = 45°$ seems to be a reasonable design (case C). The expected deterioration in performance is tied to the reduction in h_{pl}/s; (compare cases A–C in figure 19).

In order to confirm our considerations, we have built and tested the suggested surfaces with trapezoidal grooves. The experimental data can be seen in figure 20. It is obvious that, with 8.2% drag reduction, our trapezoidally grooved surfaces do not match our record blade rib configuration (9.9%). However, they are still far better than sawtooth surfaces with triangular grooves (5.1%) which had been considered to be optimal previously. Thus, trapezoidal grooves can indeed be recommended for aircraft applications.

Now what is the fuel consumption reduction which can be achieved by the implementation of riblets on aircraft? Up to 50% of the drag of a long-range aircraft consists of turbulent skin friction. Thus, the drag reduction potential for trapezoidally grooved surfaces is about 4.1%. This value is further reduced by the fact that for various reasons (dust erosion on leading edges and on some parts underneath the aircraft near the landing gear; in some locations possible destruction of riblet film by leaking hydraulic fluid; accessibility for maintenance; windows, etc.) the whole surface cannot be covered with riblet film. In addition, the riblet spacing and the riblet alignment to the flow direction may be suboptimal in some places. Therefore, an estimate for the real drag reduction potential would be 3%. What that means in terms of costs has been worked out by Airbus Industrie (Flosdorff, Roeder & Szodruch 1993). In particular, on long-range aircraft, the possible increase in payload caused by fuel savings due to riblets is most important. Its benefit is much higher than the cost savings produced by a reduction in fuel consumption alone.

8. Conclusions

We have shown in a fairly comprehensive experimental investigation how drag reduction on ribbed surfaces can be improved. For our research, a basic understanding of the theory and a specially dedicated facility that enabled us to detect very small improvements were most important. A parametric optimization was performed using surfaces with adjustable geometry. After an optimal surface configuration was found, a derivative of this configuration was selected in order to make it suitable for application to long-range commercial aircraft.

Our investigation is confined to flows with zero pressure gradient. Recent experiments hint at an improvement of riblet performance in flows with adverse pressure gradient (Nieuwstadt *et al.* 1993) or in transitional flow (Neumann & Dinkelacker 1989). In addition, we should mention that statements on fractions of a per cent drag reduction in our paper should not cause confusion. They refer only to our experimental situation. However, we do not expect dramatic changes in drag reduction for other conditions of turbulent flow. Nevertheless, we cannot exclude deviations in the 1% order for different experimental conditions.

Most of the funding for this project has been provided by the Deutsche Forschungsgemeinschaft and by the Volkswagen Foundation and is gratefully acknowledged. R. Makris built the sophisticated hardware of the adjustable plates. The Plexiglas riblet plates were designed and manufactured by Dr D. A.. Gerich. Professor P. Luchini contributed very valuable advice on the theoretical section of this paper, §6, which is mostly based on his ideas. He also provided otherwise unpublished calculations of the crossflow protrusion height of blade riblets. We thank Dr W. F. King III for a careful review of the manuscript. Finally, we appreciate the successful cooperation with Professor H. H. Fernholz and Professor H. E. Fiedler.

Appendix A. Shear stress distribution on the test plates

The turbulent flow in a rectangular channel will always produce a shear stress distribution rather than a constant shear stress level on the channel walls. Obviously, in particular in the vicinity of the corners, the deviation from the average value will be large. As a matter of fact, even in nominally parallel turbulent flows without corners, such deviations can turn out to be significant and of the order of 25% (Head & Rechenberg 1962). Therefore, we shall provide some additional shear stress data in order to support the general remarks on this issue in §2 of this paper.

In figure 21 we show wall shear stress distributions on both the test plate and on the reference plate at the opposite channel wall. The Preston tube measurements in this figure have been carried out in the middle (in the streamwise direction) of the plates. For these tests, both plates were smooth. The data have been collected at typical conditions of our drag reduction measurements, i.e at channel Reynolds number 11900 and 19000. As usual, the pressure gradient control was in operation. The latter device consists of a movable lid on top of the channel that is adjusted in height and angle in order to produce zero pressure gradient in the test section. (For technical details see Bechert *et al.* 1992). The movable lid is located relatively close to the upper edge of the test plates and thus we see a distortion of the shear stress distribution there. At this particular location with the highest deviation, the local shear stress is lowered by about 15% below the average value on the plate, $\tau_{0\,Ref}$. That causes a local reduction of u_τ by about 7% below the average value. When a riblet plate is used as a test plate, this deviation results locally in a minor horizontal shift in a drag reduction curve, because the quantity s^+ is proportional to u_τ. In order to assess that deleterious influence, one can carry out a numerical integration over an array of longitudinal slices of the test plate having variable local properties as derived from the data in figure 21. For a riblet plate, one would obtain for the resulting curve a small deviation from the one obtained with an assumed constant (average) shear stress on the plate. Actually, as it turns out, for a typical riblet plate we calculate only a 0.25% shift in maximum shear stress reduction. This shift is indeed much smaller than one would expect. It is well within our error bandwidth. However, at this point, we would like to stress that our error bandwidth, as used throughout this paper, refers to a comparative test between different surface configurations exposed to nominally identical flow conditions. As an additional check, we provide in the following a second set of data with the pressure control lid on the channel being removed, i.e. with an open channel surface. This change in channel configuration results in a very significant smoothing effect on the shear stress distribution (see figure 22).

Subsequently, with both channel configurations, we have carried out comparative shear force measurements with our balance and with a riblet surface on our test plate. (Obviously, the required reference checks with smooth plates on both sides were also

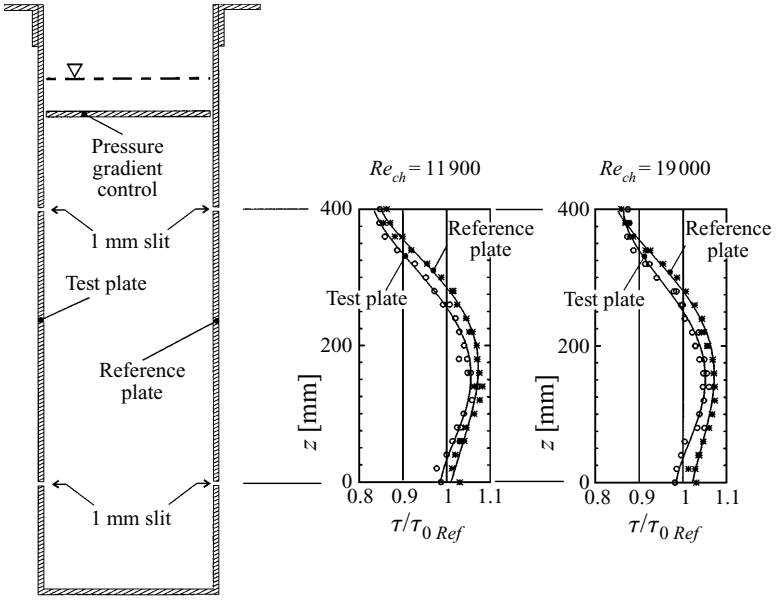

FIGURE 21. Shear stress distribution on the test plates with pressure gradient control in operation.

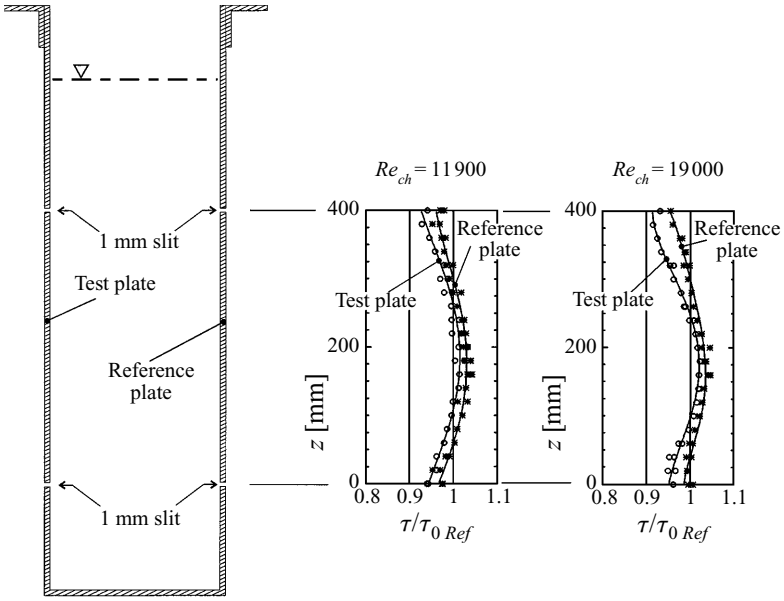

FIGURE 22. Shear stress distribution on the test plates with open channel surface.

run.) Both test series, with closed and open channel, were conducted on consecutive days in order to minimize systematic errors. As a riblet surface, we used our test plate with trapezoidal grooves. The ribs had a wedge angle of 30° and a groove depth of $h = 0.5s$ (see figure 20). The results of these comparative drag reduction measurements can be seen in figure 23. They exhibit only minimal deviations between the two channel configurations possessing quite different shear stress distributions. Thus, it is

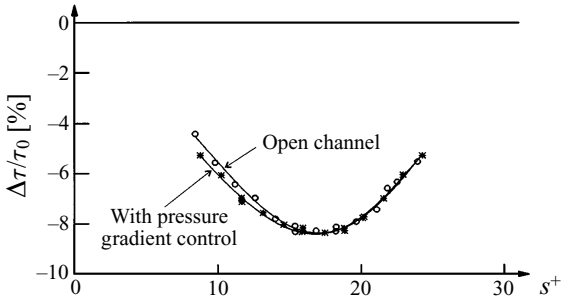

FIGURE 23. Influence of shear stress distribution on drag reduction data.

demonstrated unambiguously that the shear stress distribution on our test plates, which deviates somewhat from a constant value, has no significant impact on the drag reduction measurements.

From the data in figure 23 one is tempted to ask why a pressure gradient control is necessary at all. Nevertheless, there are good reasons for its use. Obviously, the pressure gradient of a channel flow with a free surface produces different static pressure at the front and rear ends of our test plates. Thus, forces on both end surfaces are generated which do not cancel each other. These residual forces can cause errors of the shear stress measurements of the order of 1 %. However, in the experiment shown in figure 23, the pressure forces on both the test plate and the smooth reference plate were the same owing to a symmetrical configuration of the frame of both plates. Thus, in that particular case, the error due to a pressure gradient in the streamwise direction was eliminated. However, such symmetrical configurations could not always be sustained, e.g. for our adjustable surfaces complete symmetry could not be achieved. Last, but not least, an undesired and possibly deleterious in- and outflow through the slit around the test plates is also suppressed by the pressure gradient control.

Appendix B. Test plates, technical details

One significant property of the test plates for the skin friction experiments is their shape at the leading and trailing edges. This shape is important because it can contaminate the measurements. The design should exclude additional forces on the test plates acting in the streamwise direction. These forces can be generated by distributions of (unbalanced) static pressures on the front and rear end of a test plate. The cause for this can be misalignment of the test plate and/or a static pressure gradient on the plate in the streamwise direction. In our previous wind-tunnel shear stress balance (Bechert *et al.* 1985) we picked up the static pressure distribution in the gap between the test plate and its surrounding frame. Subsequently, the gap pressure distribution which occurred was used to correct the shear force measurements.

In the present facility, however, the viscous sublayer is relatively thick, i.e. 1–4 mm. Therefore, an alignment error of the test plate height within ± 0.1 mm does not produce any serious distortions of the flow. The alignment accuracy is achieved because it is possible to warp our test plate so that it matches its frame at 3 points at both the leading and trailing edges (for the thicker adjustable plates the adjustments can be made only at 2 points on each side). In case there is a small misalignment, the ensuing build up of static pressure in the gap would lead only to very localized deviating pressure distributions. This would occur in the vicinity of the tip of the 45°

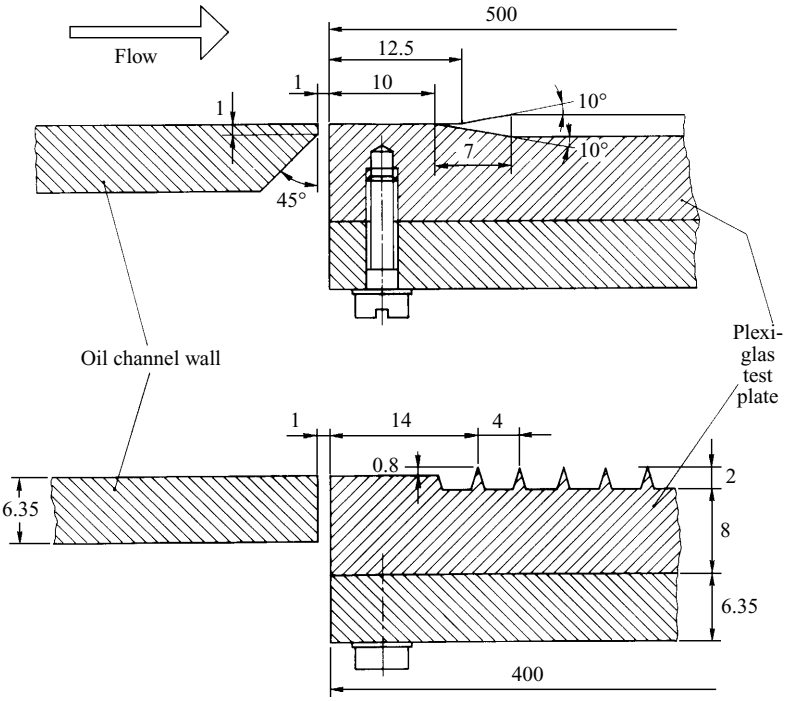

FIGURE 24. Milled Plexiglas test plate. Configuration of leading/trailing and side edge. Dimensions to scale in mm.

wedge of the oil-channel wall frame (see figure 24). Under the test plate, the static pressure is constant because the cavity underneath is very large. In addition, the pressure gradient in the flow above the test plate is balanced to zero by a movable lid on top of the test section. This lid is adjusted for each individual Reynolds number (or shaft speed of the drive unit) of the channel. The optimal lid adjustment has been determined as accurately as possible (static pressure measurements in oil are not trivial) by picking up the static pressure at three locations in front and downstream of the test plates on both sides of the channel, i.e. at 12 measuring positions. Each optimal lid adjustment was then stored in the memory of the control computer of the oil channel. With two computer-operated stepper motors the appropriate position of the lid was then adjusted during the measurements.

Measurements of shear stress are carried out with two plates on opposing sides of the oil channel. It is thus unlikely that pressure gradients in the flow have any significant effect on the shear stress measurements, in any case as long as the geometry of the frame of both plates is identical. This has been checked to be so, as we have shown in our previous description of our oil channel (Bechert *et al.* 1992).

B.1. *Milled Plexiglas plates*

Our test plates were milled with a computer controlled milling machine. Since a professional milling machine is very expensive, we used a drilling machine for electronic circuit plates (Isert Type 2571 + 3380 + 2208). The XYZ support for the milling tool was operated by stepper motors which were controlled by a personal computer. The computer control suggests a fast production. Unfortunately, this is not so. The speed at which the milling tools can operate in Plexiglas is very low. Consequently, it takes 1–2 weeks to produce one Plexiglas plate with riblets. However,

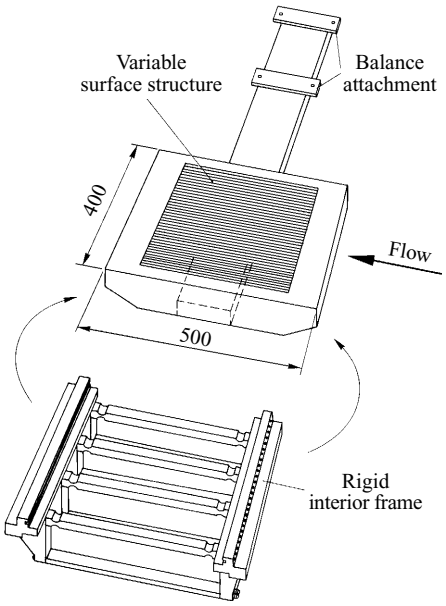

FIGURE 25. Mechanical structure of the adjustable surface. Dimensions in mm.

we have produced 20 test plates in this way, in particular those with triangular and trapezoidal grooves and those with scalloped cross-section.

Figure 24 also shows how our riblets begin and end at the leading/trailing edge. The milled riblet plate starts and ends with a smooth surface strip for better alignment. Then, there is a rather gradual transition to the actual rib structure. On most test plates we have kept the origin of the riblet velocity profile (which can be calculated) at the same elevation as the surface of the smooth surface around it. However, we could not see an effect on our data if that condition was not so well obeyed. As a matter of fact, the gradual transition between smooth plate and riblets can be replaced by an abrupt change without visible effect on the shear stress data.

B.2. *Adjustable test plates*

In figure 11 we have already shown a photograph of our adjustable test plate with slits and ribs. An additional drawing of this test plate can be seen in figure 25.

The solid interior frame of the plate has to accommodate the tension force of the 75 longitudinal blades which are each subjected to a tension of 300 N. Thus, it has to absorb 2.25 metric tons of force with an admissible deflection of about 0.1 mm. That requires a careful engineering design of the frame. The longitudinal blades are fastened individually with Allenhead screws on each end. The required tension is checked by acoustic tuning as with a harp. The harp-like blade array structure enables us to install different mechanical insertions between the blades. The insertions can be moved up and down relative to the fixed blade array. This movement is achieved with thread rods (not shown here) which are operated by a tooth belt from outside the channel oil. Obviously, the insertions have to have fine slits through which the blades can intersect.

One insertion, (i.e. the slit surface) consists of guide vanes like those of our previous glycerine experiment described in §1 (see figures 3, 10 and 11). With a lever system, the angle of the guide vanes and with it the slit width can be changed. Figure 26 shows an additional longitudinal cross-section of this slit surface.

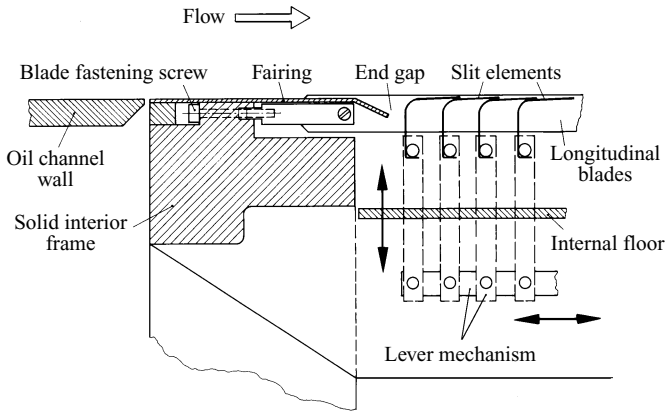

FIGURE 26. Longitudinal cross-section of the adjustable surface with slits and longitudinal blades.

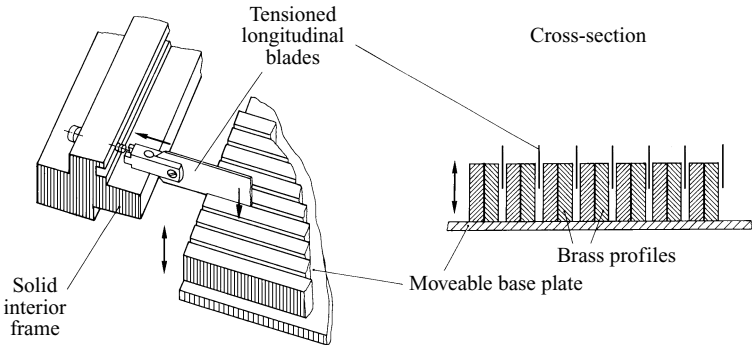

FIGURE 27. Insertion with a flat groove floor.

For the blade-riblet experiments without slits in §5, we have built another insertion. It consists of rectangular brass profiles mounted side by side (with small gaps for the blade array) onto a flat base plate. With this second insertion, a smooth groove floor could be produced. As before, the groove depth could be modified in its height. Figure 27 shows the device. As can be seen in this figure, the longitudinal brass profiles actually consist of two elements which are fastened together with small screws. This particular design enables us to clamp an additional longitudinal blade between the two halves of the rectangular brass profiles. Because the lateral distance between the blades in this arrangement is half the spacing of the tensioned blades of the 'harp' arrangement, test data at lower s^+ can be obtained. This was particularly important for our investigation of riblet behaviour at low s^+ in §6 where we used this latter arrangement.

Finally, for various blade rib experiments, we have built another test plate. Here, we have abandoned the 'harp' arrangement with tensioned longitudinal blades, but we still use the solid frame shown in figure 25. This third plate had a fixed floor and movable blades, in contrast to the previous 'harp' device where it was the other way round. The fixed floor consisted of an array of tensioned brass rods with quadratic cross-section and small longitudinal gaps between them. The blade ribs could be inserted through these gaps and were then locked onto another plate below the brass rods. This latter plate with the blade ribs could be moved up and down by a thread

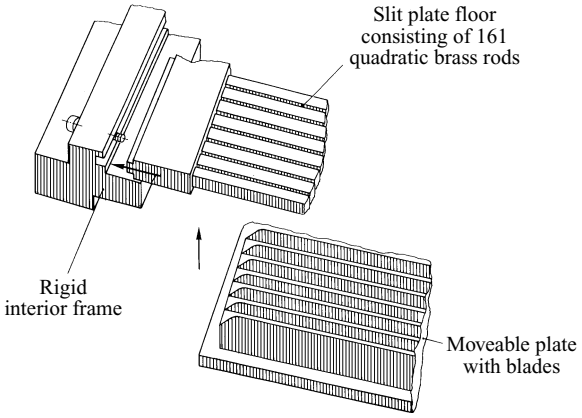

FIGURE 28. Adjustable test plate with a fixed floor and movable blades.

rod/tooth belt mechanism as before. A schematic of this third adjustable plate can be seen in figure 28. The advantage of this third adjustable test plate is that the height alignment of the blades is much more accurate (± 0.03 mm) than with our tensioned blades. In addition, blades can be exchanged much more rapidly.

A drawback of all adjustable surfaces is the deleterious effect of gaps and slits. Our tests with variable slit surfaces (§4) clearly hinted at this effect and quantified it. In particular, in the supposedly 'smooth' plate condition, when the gaps were not submerged between the longitudinal blade ribs, this had a measurable effect of the order of one per cent or so. Actually, this effect can be seen in figures 12 and 13 for the data with $h/s = 0$. It is probably mostly due to the 'end gaps' shown in figure 26 which also occurred for our second surface with a smooth groove floor (figure 27).

Obviously these end gaps can be sealed with an array of metal strips. However, in our third surface with the brass rods (figure 28), this effect did not occur, but the longitudinal slits between the brass rods still caused a problem. For one single experiment, we sealed all longitudinal slits with an oil resistant plastic strip. Indeed, this latter improvement produced the best results, as shown in figure 14.

REFERENCES

BECHERT, D. W. 1996 On the calibration of Preston tubes. *AIAA J.* **34**, 205–206.

BECHERT, D. W. & BARTENWERFER, M. 1989 The viscous flow on surfaces with longitudinal ribs. *J. Fluid Mech.* **206**, 105–129.

BECHERT, D. W., BARTENWERFER, M. & HOPPE, G. 1990 Turbulent drag reduction by nonplanar surfaces – a survey on the research at TU/DLR Berlin. In *Structure of Turbulence and Drag Reduction: IUTAM Symp., Zürich, 1989* (ed. A. Gyr), pp. 525–543. Springer.

BECHERT, D. W., BARTENWERFER, M., HOPPE, G. & REIF, W.-E. 1986 Drag reduction mechanisms derived from shark skin. Presented at *15th Congr. of the Intl Council of the Aeronautical Sciences, 7–12 September, London, UK*. ICAS-86-1.8.3. AIAA.

BECHERT, D. W., GERICH, D. A. & HOPPE, G. 1987 Short report on measurements with sawtooth riblets (3 M plastic riblet film). Internal Report, DLR Berlin.

BECHERT, D. W. & HOPPE, G. 1988 Oberflächen zur Widerstandsverminderung. Zwischenbericht zum Forschungsvorhaben Fi 178/26-1, Hermann-Föttinger-Institut, TU Berlin. The material has been also presented at the *3rd European Turbulent Drag Reduction Working Party, ONERA Chatillon, Paris, 29–30 September*.

BECHERT, D. W., HOPPE, G., HOEVEN, J. G. T. VAN DER & MAKRIS, R. 1992 The Berlin oil channel for drag reduction research. *Exps. Fluids* **12**, 251–260.

Bechert, D. W., Hoppe, G. & Reif, W.-E. 1985 On the drag reduction of the shark skin. *AIAA Paper* 85-0546.

Bruse, M., Bechert, D. W., Hoeven, J. G. T. van der, Hage, W. & Hoppe, G. 1993 Experiments with conventional and with novel adjustable drag-reducing surfaces. In *Near-Wall Turbulent Flows* (ed. R. M. C. So, C. G. Speziale & B. E. Launder), pp. 719–738. Elsevier.

Carpenter, P. W. 1995 Further developments in the use of passive porous walls for drag reduction. Presented at: *EUROMECH Colloquium 332/9th European Drag Reduction Working Meeting*, *19–20 April*, *Ravello*, *Italy*.

Choi, K.-S. 1987 Test of drag reducing riblets on a one-third scale racing yacht. Presented at *Turbulent Drag Reduction by Passive Means Conf. 15–17 September*, *London*, *UK*. Royal Aeronautical Society.

Choi, H., Moin, P. & Kim, J. 1993 Direct numerical simulation of turbulent flow over riblets. *J. Fluid Mech.* **255**, 503–539.

Coustols, E. & Cousteix, J. 1990 Experimental investigation of turbulent boundary layers manipulated with internal devices: Riblets. In *Structure of Turbulence and Drag Reduction: IUTAM Symp.*, *Zürich*, *1989* (ed. A Gyr), pp. 577–584. Springer.

Dam, W. P. van 1986 Weerstandsvermindering en een turbulente grenslag als gevolg van microgroeven. *Technische Hogeschool Delft*, *Vakgroep Stromingsleer*, *Rep*, June.

Dinkelacker, A., Nitschke-Kowsky, P. & Reif, W.-E. 1988 On the possibility of drag reduction with the help of longitudinal ridges in the walls. In *Turbulence Management and Relaminarization: IUTAM Symp.*, *Bangalore*, *India 1987* (ed. H. W. Liepmann & R. Narasimha). Springer.

Flosdorff, H., Roeder, J. & Szodruch, J. 1993 Technologische Anforderungen an Grossraumflugzeuge im Unterschallbereich, Part 2. *Luft- und Raumfahrt*, **2**, March/April, pp. 29–35.

Goldstein, D., Handler, R. & Sirovich, L. 1995 Direct numerical simulation of turbulent flow over a modelled riblet covered surface. *J. Fluid Mech.* **302**, 333–376.

Granola, H., Murcsy-Milian, H. & Tamasch, F. 1991 Errors, truncation and other deleterious effects in fluid dynamical research. *Proc. Conf. Loss Mechanisms in Aeronautics*, *1–4 April*, *Brunswick*, *Maine*, *USA*.

Head, M. R. & Rechenberg, I. 1962 The Preston tube as a means of measuring skin friction. *J. Fluid Mech.* **14**, 1–17.

Higdon, J. J. L. 1985 Stokes flow in arbitrary two-dimensional domains: shear flow over ridges and cavities. *J. Fluid Mech.* **159**, 195–226.

Higdon, J. J. L. 1990 Effect of pressure gradients on Stokes flows over cavities. *Phys. Fluids* A **2**, 112–114.

Hoeven, J. G. T. van der & Bechert, D. W. 1991 Experiments with a 1:4.2 model of a commuter aircraft with riblets in a large windtunnel. In *Recent Developments in Turbulence Management* (ed. K.-S. Choi), pp. 3–24. Kluwer.

Kramer, M. O. 1939 Einrichtung zur Verminderung des Reibungswiderstandes, Patentschrift 669897, Klasse 62b, Gruppe 408. Patentiert vom 17. März 1937 an.

Luchini, P. 1992 Effects of riblets on the growth of laminar and turbulent boundary layers. Presented at *The 7th European Drag Reduction Meeting*, *24–25 September*, *Berlin*, *Germany*.

Luchini, P., Manzo, F. & Pozzi, A. 1991 Resistance of a grooved surface to parallel flow and cross-flow. *J. Fluid Mech.* **228**, 87–109.

Luchini, P., Manzo, F. & Pozzi, A. 1992 Viscous eddies over a grooved surface computed by a Gaussian-integration Galerkin boundary-element method. *AIAA J.* **30**, 2168–2170.

McLean, J. D., George-Falvy, D. N. & Sullivan, P. P. 1987 Flight-test of turbulent skin-friction reduction by riblets. In *Turbulent Drag Reduction by Passive Means*, *Conference*, *15–17 September*, *London*, *UK*. Royal Aeronautical Society.

Marentic, F. J & Morris, T. L. 1986 Drag reduction article. European Patent Application by the 3 M Company, St Paul, Minnesota; Application No. 86304131.5 Int. Cl. B 64C21/10; B 05 D 5/02. Priority 31.05.85 US 740239.

Neumann, D. & Dinkelacker, A. 1989 Drag reduction by longitudinal riblets on the surface of a streamwise aligned body of revolution. In *Drag Reduction in Fluid Flows*, *31 July–3 August 1989*, *Davos*, *Switzerland* (ed. R. H. J. Sellin & R. T. Moses), pp. 93–98. Ellis Horwood.

NIEUWSTADT, F. T. M., HOEVEN, J. G. TH. VAN DER, LEIJDENS, H. & KRISHNA PRASAD, K. 1989 Some experiments on riblet surfaces in a towing tank. In *Drag Reduction in Fluid Flows*, *31 July–3 August 1989*, *Davos*, *Switzerland* (ed. R. H. J. Sellin & R. T. Moses), pp. 85–92. Ellis Horwood.

NIEUWSTADT, F. T. M., WOLTHERS, W., LEIJDENS, H., KRISHNA PRASAD, K. & SCHWARZ-VAN MANEN, A. 1993 The reduction of skin friction by riblets under the influence of an adverse pressure gradient. *Exps. Fluids* **15**, 17–26.

NITSCHKE, P. 1983 Experimentelle Untersuchung der turbulenten Strömung in glatten und längsgerillten Rohren. Max-Planck-Institut für Strömungsforschung, Bericht 3/1983.

ROHR, J., ANDERSON, G. W. & REIDY, L. W. 1989 An experimental investigation of the drag reducing effects of riblets in pipes. In *Drag Reduction in Fluid Flows*, *31 July–3 August*, *Davos*, *Switzerland* (ed. R. H. J. Sellin & R. T. Moses), pp. 263–270. Ellis-Horwood.

SAWYER, W. G. & WINTER, K. G. 1987 An investigation of the effect on turbulent skin friction of surfaces with streamwise grooves. In *Turbulent Drag Reduction by Passive Means, Conf. 15–17 September*, *London*, *UK*. Royal Aeronautical Society.

SCHLICHTING, H. 1979 *Boundary Layer Theory* (trans. J. Kestin), 7th edn. McGraw-Hill.

SUZUKI, Y. & KASAGI, N. 1994 Turbulent drag reduction mechanism above a riblet surface. *AIAA J.* **32**, 1781–1790.

TANEDA, S. 1979 Visualization of separating Stokes flows. *J. Phys. Soc. Japan* **46**, 1935–1942.

TAKEMATSU, M. 1966 Slow viscous flow past a cavity. *J. Phys. Soc. Japan* **21**, 1816–1821.

WALSH, M. J. 1980 Drag characteristics of V-groove and transverse curvature riblets. In *Viscous Flow Drag Reduction* (ed. G. R. Hough), Progress in Astronautics and Aeronautics, vol. 72, pp. 168–184. AIAA.

WALSH, M. J. 1982 Turbulent boundary layer drag reduction using riblets. *AIAA Paper* 82-0169.

WALSH, M. J. 1983 Riblets as a viscous drag reduction technique. *AIAA J.* **21**, 485–486.

WALSH, M. J. 1990 Riblets. In *Viscous Drag Reduction in Boundary Layers*. (ed. D. M. Bushnell & J. N. Hefner), Progress in Astronautics and Aeronautics, vol. 123, 203–261. AIAA.

WALSH, M. J. & LINDEMANN, A. M. 1984 Optimization and application of riblets for turbulent drag reduction. *AIAA Paper* 84-0347.

WALSH, M. J., SELLERS, W. L. & MCGINLEY, C. B. 1989 Riblet drag reduction at flight conditions. *J. Aircraft* **26**, 570–575.

WEI, T. & WILLMARTH, W. W. 1989 Reynolds-number effects on the structure of a turbulent channel flow. *J. Fluid Mech.* **204**, 57–95.

WEISS, M. H. 1993 Drag reduction with riblets in pipe flow. PhD Diss., University of Calgary, Alberta, Canada.

WILKINSON, S. P. & LAZOS, B. S. 1988 Direct drag and hot-wire measurements on thin-element riblet arrays. In *Turbulence Management and Relaminarization: IUTAM Symp.*, *Bangalore*, *India*, *1987* (ed. H. W. Liepmann & R. Narashimha). Springer.